

Mechanism-based Tuning of Room-temperature Ferromagnetism in Mn-doped β -Ga₂O₃ by Annealing Atmosphere

Xu Dai, Xi Zhang, Gang Xiang*

College of Physics, Sichuan University, Chengdu 610000, China.

*Corresponding email: gxiang@scu.edu.cn

ABSTRACT

Mn-doped β -Ga₂O₃ (GMO) films with room-temperature ferromagnetism (RTFM) are synthesized by polymer-assisted deposition and the effects of annealing atmosphere (air or pure O₂ gas) on their structures and physical properties are investigated. The characterizations show that the concentrations of vacancy defects and Mn dopants in various valence states and lattice constants of the samples are all modulated by the annealing atmosphere. Notably, the samples annealed in air (GMO-air) exhibit a saturation magnetization as strong as 170% times that of the samples annealed in pure O₂ gas (GMO-O₂), which can be quantitatively explained by oxygen vacancy (V_O) controlled ferromagnetism due to bound magnetic polarons established between delocalized hydrogenic electrons of V_Os and local magnetic moments of Mn²⁺, Mn³⁺, and Mn⁴⁺ ions in the samples. Our results provide insights into mechanism-based tuning of RTFM in Ga₂O₃ and may be useful for design, fabrication, and application of related spintronic materials.

KEYWORDS

Mn-doped β -Ga₂O₃; Annealing atmosphere; Oxygen vacancies; Room temperature ferromagnetism; Bound magnetic polaron.

1. INTRODUCTION

Owing to the co-existence of charge and spin degrees of freedom in the diluted magnetic semiconductors (DMSs), tremendous attention has been aroused in semiconductor spintronics.¹⁻⁴ As a promising wide-bandgap material that has been studied for a long time for various applications including solar-blind detectors and high-frequency power devices,^{5,6} very recently gallium oxide (Ga_2O_3) has attracted much interest for its potentials in spintronic applications.⁷⁻¹⁰ It is found that the ferromagnetism (FM) in Ga_2O_3 can be realized by doping with various metallic elements, such as Fe^{11} , Ni^{12} , Cr^{13} , Sn^{14} and Mn^{15-22} . Among them, Mn is the most investigated dopant in Ga_2O_3 . For instance, Hayashi *et al.* observed room-temperature ferromagnetism (RTFM) in Mn-doped γ - Ga_2O_3 which was considered to be related to holes in the mid-gap Mn band.¹⁵ Pei *et al.* reported that the RTFM in Mn-doped β - Ga_2O_3 could be explained by carrier-mediated double exchange model.¹⁶ However, Guo *et al.* found that highly resistive Ga_2O_3 could not provide enough mobile carriers to induce the FM in double exchange model, and the FM in Mn-doped β - Ga_2O_3 should come from the coupling between Mn ions and oxygen vacancies (V_{Os}) since both saturation magnetization (M_s) and coercive field (H_C) increased with the concentration of Mn dopants (Mn^{2+} and Mn^{3+} ions).¹⁷ The calculations based on density functional theory suggested that the RTFM of Mn-doped β - Ga_2O_3 should come from the strong p - d coupling and the delocalization of O-2 p orbitals.¹⁸ Very recently, Peng *et al.* reported that both FM and antiferromagnetism (AFM) existed in the Mn^+ ion-implanted β - Ga_2O_3 , where FM was related to the coupling of Ga vacancies (V_{Gas}) in the high resistance

region and AFM came from MnO phases in the samples.¹⁹ Obviously, although much work has been done on ferromagnetic Mn-doped Ga₂O₃, the mechanism underlying the ferromagnetism remains controversial. Therefore, for both basic science and potential applications, it is important and necessary to further investigate the mechanism by modulating the concentrations of vacancy defects and various Mn ions in different valence states and their possible couplings in Ga₂O₃.

In this work, Mn-doped β -Ga₂O₃ (GMO) pre-films are first prepared by polymer-assisted deposition (PAD) and then annealed in air atmosphere and pure O₂ gas to obtain GMO-air and GMO-O₂ polycrystalline thin films, respectively. The structures and concentrations of various Mn in different valence states (Mn²⁺, Mn³⁺ and Mn⁴⁺ ions) and vacancy defects of the obtained films are characterized and the effects of annealing atmosphere on the magnetic, optical, and electrical properties of the films are then investigated.

2. EXPERIMENTAL DETAILS

2.1 Specimen preparation

The polyethyleneimine (PEI) ((M.W. 10,000, 99%, Sigma-Aldrich) and Ethylene Diamine Tetraacetic Acid (EDTA) (99.9%, Sigma-Aldrich) are added to deionized water in a certain proportion to prepare the polymer solution. Subsequently, gallium nitrate hydrate (GaN₃O₉·xH₂O, 99.9%, Sigma-Aldrich) is added to the polymer solution to obtain Ga-polymers solution, and manganese chloride tetrahydrate (MnCl₂·4H₂O, 99.9%, Sigma-Aldrich) is added to the polymer solution to obtain Mn-polymers solution. Then the unbound ions need to be filtered out from the Ga-polymers

solution and the Mn-polymers solution by Amicon cells. The Mn-doped Ga precursor (GaMn-polymers) solution is prepared by adding the Mn-polymers solution to the Ga-polymers solution, which is then dropped on single crystalline *c*-plane sapphire substrate to prepare pre-films using 30s-spin-coating at 3000 rpm. The GaMn-polymers are tested by thermalgravimetric analysis and differential scanning calorimeter (TGA-DSC) (TA instruments, Q40) to study the changes of weight and calorie during annealing in air and pure O₂ gas. Figure 1(a) shows the TG and DSC curves of the GaMn-polymers in air. The exothermic peaks at 290°C and 484°C represent the decompositions of the GaMn-polymers, and the endothermic peak at 588°C represents the crystallization of Mn-doped gallium oxide. The TG and DSC curves in pure O₂ gas show similar results. Based on the TG-DSC results, the pre-films are heated up to 550 °C for 1 h to completely decompose PEI and EDTA, and then annealed in air and pure O₂ gas at 750°C to obtain GMO-air and GMO-O₂ films, respectively. The annealing in oxygen-rich conditions is necessary for obtaining crystalline samples.²³ The large-scale (~2cm×2cm) GMO-air and GMO-O₂ films are translucent brown, as shown in in Figure 1(b). By changing the concentration of the precursor solution and the number of suspension coatings, dozens to hundreds of nanometer-thick GMO films are obtained. For comparison, undoped β-Ga₂O₃ films are also prepared.

2.2 Characterization

The morphologies of the GMO films are depicted by atomic force microscope (AFM, Benyuan, CSPM5500). X-ray diffraction (XRD, Bruker D8, Empyrean analytical diffractometer) using a Cu K α radiation source and high-resolution transmission

electron microscopy (HRTEM, Titan Themes Cubed G2 300) are used to characterize crystalline structures. Cross-sectional samples for TEM are prepared by focus ion beam (FIB) milling in a Helios system (Tescan, LYRA 3 XMU). Elemental composition and valence are examined by X-ray photoelectron spectroscopy (XPS, Kratos AXIS Supra). Optical properties are evaluated using UV-visible spectrophotometer (PerkinElmer Lambda 950 UV-Vis-NIR) and photoluminescence (PL, LS-45). Magnetic and electrical properties are measured by Superconducting Quantum Interference Devices (SQUID, Quantum Design, MPMS-XL-5) and four-probe resistivity tester (FPPRT, ST-2722), respectively.

3. RESULTS AND DISCUSSION

3.1 Structural Properties

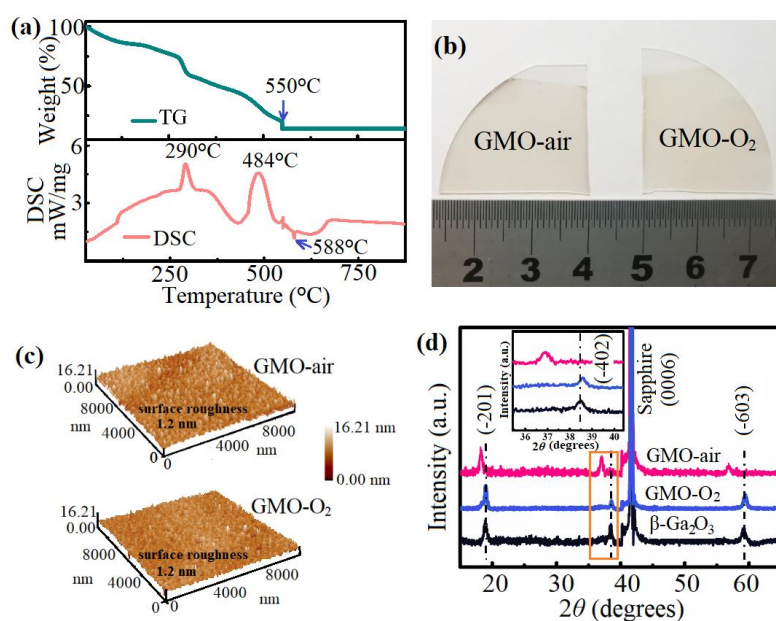


FIGURE 1 (a) TG and DSC curves of the GaMn-polymers in the air. (b) The digital photos of the GMO films grown on the sapphire substrates. (c) 3D AFM images of the GMO films grown on the sapphire substrates. (d) XRD patterns of the PAD-grown

GMO-air, GMO-O₂ and undoped β -Ga₂O₃ films on the *c*-plane sapphire. The inset is the enlarged view of XRD patterns around 38°.

The three-dimensional atomic force microscope images in Figure 1(c) indicate that the surface roughness of the GMO films is ~ 1.2 nm. The crystal structures of the obtained films are studied by XRD. As shown in Figure 1(d), three diffraction peaks belong to (-201), (-402), and (-603) groups of β -Ga₂O₃ are observed in the samples, indicating the (-201) preferential growth orientation of the films.²² The GMO-air and GMO-O₂ films are composed of poly crystals with an average diameter around 20.7 nm and 31.2 nm, respectively, estimated by the Scherrer formula. Importantly, no peaks of Mn-related secondary phases (clusters, oxides or compounds) are observed, because the metallic elements (Ga and Mn) are uniformly mixed in the polymers during the PAD process^{23, 24} and Mn-related secondary phases are difficult to form in β -Ga₂O₃.^{17, 20} The observation of single β phase of Ga₂O₃ is consistent with the single crystallization peak in the DSC curve of the GaMn-polymers in Figure 1(a). The inset is the enlarged view of θ -2 θ XRD patterns around 38°. Interestingly, comparing with those of undoped β -Ga₂O₃, the diffraction peaks of GMO-O₂ are just slightly right-shifted, while the diffraction peaks of GMO-air are dramatically left-shifted. The (-402) inter-planar spacing values of un-doped, GMO-O₂ and GMO-air can be calculated using the Bragg equation and obtained as 0.232 nm, 0.230 nm and 0.240 nm, respectively. Since the size order of the cation radii in the GMO films are as follows: Mn²⁺ (0.83 Å) > Mn³⁺ (0.64 Å) > Ga³⁺ (0.62 Å) > Mn⁴⁺ (0.53 Å),¹⁷ the slightly smaller inter-planar spacing of

GMO-O₂ and the much larger inter-planar spacing of GMO-air indicate that more Mn⁴⁺ ions are incorporated in GMO-O₂ and more Mn²⁺ ions are incorporated in GMO-air, which will be quantitatively confirmed by the HRTEM and XPS results later.

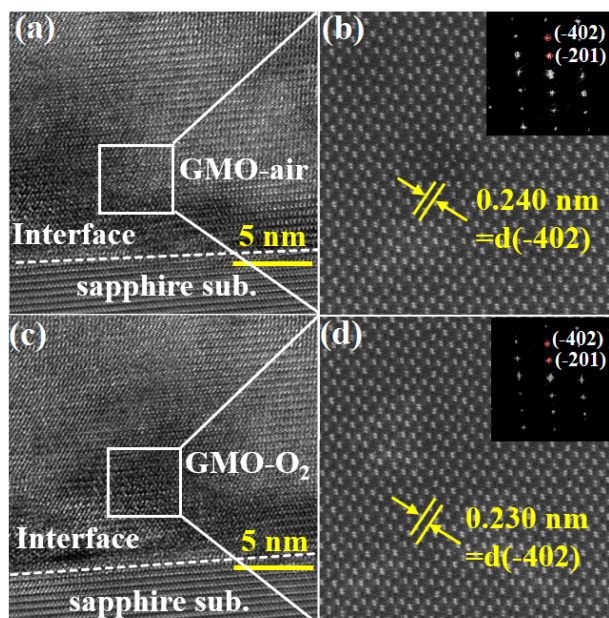


FIGURE 2 (a) Cross-sectional HRTEM image of GMO-air film. (b) Spherical aberration TEM image of GMO-air film. (c) Cross-sectional high-resolution TEM image of GMO-O₂ film. (d) Spherical aberration TEM image of GMO-O₂ film. The insets show the corresponding FFT.

The microstructures of the GMO films are further investigated by HRTEM. The Cross-sectional HRTEM images of the GMO-air and GMO-O₂ films are shown in Figures 2(a) and 2(c), respectively. The corresponding spherical aberration HRTEM images of the GMO-air and GMO-O₂ films are shown in Figures 2(b) and 2(d), respectively. Both the GMO-air and GMO-O₂ films are highly crystalline and grown along the direction of (-201), consistent with the XRD results. Clear crystalline

structures can be seen and no Mn-related clusters or precipitates are observed in both cases. The inter-planar spacings along (-402) azimuth of the GMO-air and GMO-O₂ films are about 0.240 nm and 0.230 nm, respectively, consistent with the XRD results.

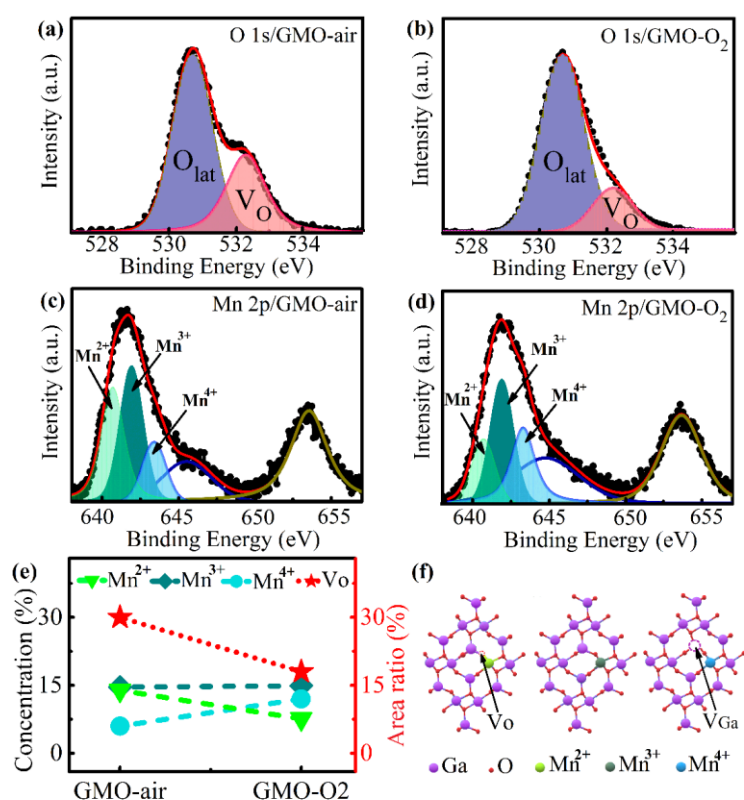


FIGURE 3 O 1s peaks of (a) GMO-air and (b) GMO-O₂. Mn 2p peaks of (c) GMO-air and (d) GMO-O₂. (e) The doping concentrations of different Mn ions and the area ratio of V_Os-related peak in the GMO films. (f) The schematic diagram of formation of Mn²⁺, Mn³⁺ and Mn⁴⁺ ions in Ga₂O₃.

The chemical states of the elements in the GMO films are studied by XPS. By fitting the XPS whole scanning spectra (not shown), the atomic ratios between oxygen and cation of GMO-air and GMO-O₂ films are obtained as 1.42 and 1.45, respectively. The stoichiometric ratio is less than 1.5 in Ga₂O₃, indicating the existence of vacancy defects.

As shown in Figures 3(a) and (b), each O 1s peak of GMO-air and GMO-O₂ could be fitted into two sub-peaks located at 530.7 eV and 532.1 eV, corresponding to O ions surrounded by metal atoms (O_{lat}) and V_Os in the metal bonding matrix, respectively.^{24,25} The area ratio of V_Os-related peak of GMO-air and GMO-O₂ are estimated to be 30% and 18%, respectively, indicating that there are more V_Os in GMO-air. The Mn doping concentrations in GMO-air and GMO-O₂ both are about 34.5%, estimated by fitting the XPS whole scanning spectra. Figures 3(c) and (d) show the Mn 2p spectra of the GMO-air and GMO-O₂ films, respectively. The main peak can be fitted into three sub-peaks located at about 640.6 eV, 641.8 eV and 643.2 eV, corresponding to Mn²⁺, Mn³⁺ and Mn⁴⁺ ions, respectively.^{17, 26} The concentrations of Mn²⁺, Mn³⁺ and Mn⁴⁺ ions in GMO-air are obtained as 13.9%, 14.6% and 6.0%, respectively, while the concentrations of Mn²⁺, Mn³⁺ and Mn⁴⁺ ions in GMO-O₂ are 7.6%, 14.9% and 12.0%, respectively. The doping concentrations of different Mn ions and the area ratio of V_Os-related peak are shown in Figure 3(f). Much more Mn²⁺ ions in GMO-air are responsible for the increase of inter-planar spacing shown in Figure 1(d). Meanwhile, more Mn⁴⁺ ions in GMO-O₂ are responsible for the decrease of inter-planar spacing shown in Figure 1(d). In general, substitutional Mn dopants in Ga₂O₃ mainly exist as Mn³⁺ ions when there are no other defects around.¹⁸ When there is a V_O nearby a Mn³⁺ ion, two extra electrons are introduced in the β-Ga₂O₃ lattice, one of which enters the Mn d-shell and convert the Mn³⁺ ion into an Mn²⁺ ion.^{18,26} When there is a V_{Ga} nearby a Mn³⁺ ion, the V_{Ga} acts as an acceptor and captures a 3d electron from the Mn d-shell, converting the Mn³⁺ ion into an Mn⁴⁺ ion.^{18,26} The schematic of formation of Mn²⁺, Mn³⁺ and Mn⁴⁺ ions in the

GMO films is shown in Figure 3(e). It is worthwhile noting that this is the first time that Mn^{4+} ions are observed in Mn-doped Ga_2O_3 . Based on the assumption that one Mn^{4+} ion corresponds to one V_{Ga} , the higher concentration of Mn^{4+} ions in GMO- O_2 means higher V_{Ga} concentration in GMO- O_2 , which is reasonable since pure O_2 provide more oxygen than air.

3.2 Optical and Ferromagnetic Properties

Figure 4(a) shows the optical transmittance measured by UV-visible spectrophotometer of the GMO films. The GMO-air film exhibits slightly lower optical transmittance than that of the GMO- O_2 film, consistent with the results observed in Figure 1(b). The inset is the $(ah\nu)^2$ versus $h\nu$ plot of the GMO films. By fitting the plot of $(ah\nu)^2$ versus $h\nu$, the band gaps of GMO-air and GMO- O_2 are obtained as 4.98 eV and 5.18 eV, respectively. It is more V_{O} s in GMO-air that results in lower optical transmittance and smaller band gap, owing to the contributions of more occupied defect levels.^{27,28} Figure 4(b) shows the PL spectra of the GMO films. The emission band can be divided into four bands centered at about 345 nm, 415 nm, 440 nm and 480 nm, respectively. The ultraviolet emission band located at about 345 nm corresponds to the recombination of self-trapped excitons, which is an intrinsic process.²⁹ The emission peaks centered at 415 nm, 440 nm (violet light) and 480 nm (blue light) are originated from the electron-hole recombination formed by V_{O} s, or from the recombination of Ga-O vacancy pair.^{30,31} The PL intensity at the violet and blue light regions of the GMO-air films are stronger than that of GMO- O_2 films, which can be attributed to more defects such as V_{O} s in the GMO-air films. The electrical measurements show that the

resistivity values of the GMO-air and GMO-O₂ films are $1.2 \times 10^4 \Omega \cdot \text{cm}$ and $9.1 \times 10^4 \Omega \cdot \text{cm}$, respectively, and the majority carriers are electrons (n-type), which can be roughly explained by the fact that more V_{OS} exist in GMO-air films since V_{OS} act as donor-type defects to provide electrons in Ga₂O₃. In short, the tuning of the optical and electrical properties is mainly resulted from the large difference between the V_O concentrations in the GMO-air and GMO-O₂ films.

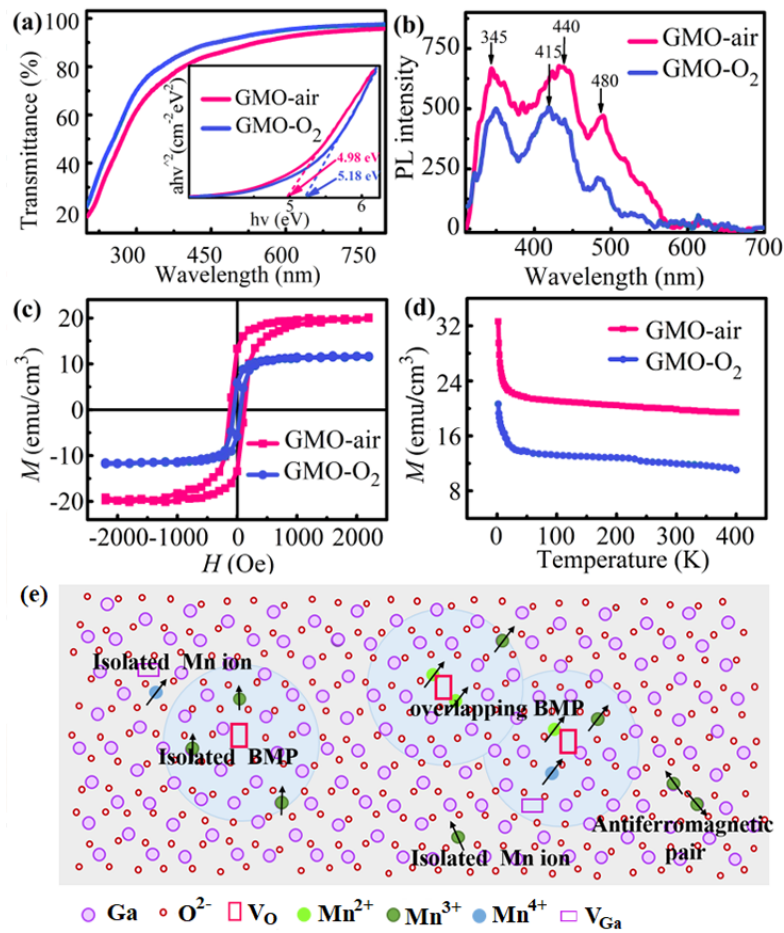


FIGURE 4 (a) Optical transmittance spectra of the GMO films. Inset is the $(ah\nu)^2$ versus $h\nu$ plot. (b) Room-temperature PL spectra of the GMO films excited at 250 nm. (c) M-H curves of the GMO films at 300 K. (d) Temperature-dependent magnetization of the GMO films. (e) Schematic of bound magnetic polarons in the GMO films.

Finally, the magnetic properties of the GMO samples are investigated. Figure 4(c) shows the magnetic field dependent magnetization ($M-H$) curves of the GMO films obtained at 300 K. During the $M-H$ measurements, H is applied in plane which is parallel to the easy magnetic axis of Mn-doped β -Ga₂O₃ films preferentially grown along the (-201) orientation.²⁰ Both GMO films display typical hysteresis loops, which are clear signals of ferromagnetism. The M_S values of the GMO-air and GMO-O₂ films are 19.7 emu/cm³ and 11.6 emu/cm³, respectively. The H_C values of the GMO-air and GMO-O₂ films are 120 Oe and 58 Oe, respectively. Obviously, GMO-air exhibits stronger M_S and H_C values, 1.7 and 2.1 times those of GMO-O₂, respectively. The temperature-dependent magnetization ($M-T$) curves of the GMO-air and GMO-O₂ films measured in field-cooling mode under 2000 Oe are shown in Figure 4(d), indicating ferromagnetism up to temperatures higher than 400 K. The magnetizations of both samples increase very slowly from 400 K down to 20 K, and then increase steeply at temperatures lower than 20 K, which could be ascribed to the presence of paramagnetic components inducing additional magnetization at low temperatures.¹⁵ Notably, the $M-T$ curves also reveal much stronger magnetization in GMO-air films than that in GMO-O₂ films.

To understand the difference between the ferromagnetic properties in the GMO-air and GMO-O₂ films, we should point out that the ferromagnetism comes from bound magnetic polarons (BMPs)³² which are closely related to the V_O defects in the GMO films. In the β -Ga₂O₃ lattice, a V_O acts as a donor and provides two additional electrons confined in hydrogenic orbitals.³³ When the donor concentration exceeds a critical

value, the hydrogenic orbitals overlap to form impurity bands, making the localized hydrogenic electrons become delocalized. The overlap between the delocalized electrons and local spin moments of Mn ions within the hydrogenic orbitals leads to ferromagnetic exchange coupling between them to form BMPs,³³ as shown Figure 4(e). When the amount of BMPs is sufficient, percolation occurs and ferromagnetic ordering is spontaneously induced. It is noted that Mn ions not included in hydrogenic orbitals will not participate in ferromagnetic exchange coupling. In addition, V_{Ga} may produce weak local spin moments, but it is difficult for them to form long-range magnetic ordering.¹⁰ In short, the ferromagnetism mainly depends on the concentrations of V_{O} s and Mn ions that are coupled with each other. According to Hund's rule, the spins contributed by an Mn^{2+} , an Mn^{3+} and an Mn^{4+} ion are 4/2, 5/2 and 4/2, respectively.^{33,34} In other words, an Mn^{2+} and an Mn^{4+} ion provide the same local spin moment, while an Mn^{3+} ion provides more local spin moment than the other two. Interestingly, GMO-air and GMO- O_2 have approximately the same concentration of Mn^{3+} ions and same concentration of total Mn dopants. This means that, if the V_{O} concentration was high enough so that all the Mn ions were included in hydrogenic orbitals, GMO-air and GMO- O_2 would exhibit the same magnetization, which obviously is not the case in our work. In fact, the V_{O} concentration is much lower than the concentration (~34.5%) of all the Mn ions in the GMO films. In this situation, the magnetization is determined by the V_{O} concentration but not the concentration of the Mn ions, and the much stronger magnetization in GMO-air can only be ascribed to much more V_{O} s in it. Notably, the V_{O} concentration in GMO-air is 1.7 times that in GMO- O_2 , quantitatively consistent

with the ratio (1.7) of the M_s of GMO-air over that of GMO-O₂. Furthermore, the greater H_C in GMO-air is also ascribed to more V_{OS}, since H_C increases with the increase of pinning sites originated from V_{OS} in oxide films.^{35,36}

4. CONCLUSIONS

The Mn-doped β -Ga₂O₃ films with RTFM are prepared by PAD and the effects of annealing atmosphere on their structures and physical properties are studied. Our results show that the RTFM comes from V_O-controlled BMPs established between sufficient delocalized electrons from V_{OS} and local spin moments of Mn various ions, and dramatical (1.7 times) tuning of the ferromagnetism can be realized based on the ferromagnetism mechanism by annealing atmosphere. Our results provide insights into the defect-controlled ferromagnetism in β -Ga₂O₃ and may be useful for related electronic and spintronic applications.

ACKNOWLEDGMENT

We are grateful to the National Natural Science Foundation of China (Grant No. 52172272). We thank the Analytical & Testing Center of Sichuan University for the XRD and XPS measurements.

REFERENCES

1. Fusil S, Garcia V, Barthélémy A, Bibes M Magnetoelectric Devices for Spintronics. *Annu. Rev. Mater. Res.* 2014, 44: 91-116.
2. Dorpe P, Liu Z, Roy W et al. Very high spin polarization in GaAs by injection from a (Ga,Mn)As Zener diode, *Appl. Phys. Lett.* 2004, 84: 3495-3497.

3. Li Z, Bai W, Li Y et al. Coexistence of large positive and negative magnetoresistance in $\text{Cr}_2\text{Si}_2\text{Te}_6$ ferromagnetic semiconductor. *Sci. China Mater.* 2021, 65:780-787.
4. Liu Y, Wang G, Wang S et al. Defect-Induced Magnetism in Neutron Irradiated 6H-SiC Single Crystals. *Phys. Rev. Lett.* 2011, 106, 087205.
5. Kong WY, Wu GA, Wang KY et al. Graphene-beta- Ga_2O_3 Heterojunction for Highly Sensitive Deep UV Photodetector Application [J], *Adv. Mater.* 2016, 28:10725.
6. Higashiwaki M, Jessen GH, Guest Editorial: The dawn of gallium oxide microelectronics . *Appl. Phys. Lett.* 2018, 112: 060401.
7. Neal AT, Zhang Y, Elhamri S, et al. Zeeman spin-splitting in the (010) β - Ga_2O_3 two-dimensional electron gas. *Applied Physics Letters*, 2019, 115:262103.
8. Conrad F, Bauer M, Weyeneth S, et al. Hierarchically structured copper gallium spinels through microwave hydrothermal methods[J]. *Solid State Sciences*, 2013, 24:125-132.
9. Higashiwaki M, Sasaki K, Murakami H et al. Recent progress in Ga_2O_3 power devices [J], *Semicond. Sci. Tech.* 2016, 31: 034001.
10. Yang Y, Zhang J, Hu S et al. First-principles study of Ga-vacancy induced magnetism in β - Ga_2O_3 , *Phys. Chem. Chem. Phys.* 2017, 19: 28928-28935.
11. Huang Y, Gao A, Guo D et al. Fe doping-stabilized γ - Ga_2O_3 thin films with a high room temperature saturation magnetic moment. *J. Mater. Chem. C* 2020, 8: 536-542.
12. Ye S, Zhang Y, He H, Qiu J, Dong G Simultaneous broadband near-infrared emission and magnetic properties of single phase Ni^{2+} -doped β - Ga_2O_3 nanocrystals via mediated phase-controlled synthesis[J]. *J. Mater. Chem. C* 2015, 3: 2886-2896.

13. Guo D, Wu Z, Li P et al. Magnetic anisotropy and deep ultraviolet photoresponse characteristics in Ga₂O₃:Cr vermicular nanowire thin film nanostructure[J]. Rsc. Adv. 2015, 5: 12894-12898.
14. Chikoidze E, Bardeleben H, Akaiwa K et al. Dumont, Electrical, optical, and magnetic properties of Sn doped α -Ga₂O₃ thin films. J. Appl. Phys. 2016, 120: 025109.
15. Hayashi H, Rong H, Ikeno H et al. Room temperature ferromagnetism in Mn-doped gamma-Ga₂O₃ with spinel structure[J]. Appl. Phys. Lett. 2006, 89: 181903.
16. Pei G, Xia C, Dong Y et al. Studies of magnetic interactions in Mn-doped β -Ga₂O₃ from first-principles calculations[J]. Scripta Mater. 2008, 58: 943-946.
17. Guo D, Wu Z, An Y et al. Room temperature ferromagnetism in (Ga_{1-x}Mn_x)₂O₃ epitaxial thin films[J]. J. Mater. Chem. C 2015, 3: 1830-1834.
18. Wang X, Quhe R, Zhi Y et al. The electronic structure and magnetic property of the Mn doped β -Ga₂O₃[J]. Superlattice. Microst. 2019, 125: 330-337.
19. Peng B, Zhang Y, Wang Y et al. Observation of room temperature ferromagnetism and exchange bias in a ⁵⁵Mn⁺ ion-implanted unintentionally doped β -Ga₂O₃ single crystal[J]. J. Magn. Magn. Mater. 2020, 506: 166687.
20. Huang Y, Chen Z, Zhang X et al. The structure and magnetic properties of β -(Ga_{0.96}Mn_{0.04})₂O₃ thin film [J]. J. Semicond. 2018, 39: 053002.
21. Rong H, Hayashi H, Oba F, Tanaka I Microstructure of Mn-doped γ -Ga₂O₃ epitaxial film on sapphire (0001) with room temperature ferromagnetism[J]. Journal of Applied Physics, 2007, 101: 063526.

22. Tang C, Sun J, Lin N et al. Electronic structure and optical property of metal-doped Ga₂O₃: a first principles study[J]. Rsc Advances, 2016, 6: 78322-78334.
23. Jia QX, McCleskey TM, Burrell AK Polymer-assisted deposition of metal-oxide films [J], Nat. Mater. 2004, 3: 529-532.
24. Dai X, Zheng Q, Zhang X, Wang Y, Xiang G High performance photoresponse of transparent β -Ga₂O₃ film prepared by polymer-assisted deposition[J]. Mater. Lett. 2021, 284:128912.
25. Yang CC, Huang JQ, Chen KY et al. Effect of Oxygen Concentration Ratio on a Ga₂O₃-based Resistive Random Access Memory[J]. IEEE Access, 2019, 7:175186-175191.
26. Guo D, Li P, Wu Z et al. Inhibition of unintentional extra carriers by Mn valence change for high insulating devices[J]. Sci. Rep-UK 2016, 6: 24190.
27. Liu H, Zeng F, Lin Y, Wang G, Pan F Correlation of oxygen vacancy variations to band gap changes in epitaxial ZnO thin films. Appl. Phys. Lett. 2013, 102:181908.
28. Zhou Q, Tao X, Di G, Shang Y, Dong L SO₂ Tolerance and Mechanism of Elemental Mercury Removal from Flue Gas by a Magnetic Recyclable Fe₆Mn_{0.8}Ce_{0.2}O_y Sorbent[J]. Energ. Fuel. 2021, 35: 5101-5109.
29. Rafique S, Han L, Zhao H Thermal annealing effect on β -Ga₂O₃ thin film solar blind photodetector heteroepitaxially grown on sapphire substrate[J]. Phys. Status Solidi A 2017, 214: 1700063.
30. Binet L, Gourier D Origin of the blue luminescence of β -Ga₂O₃. J. Phys. Chem. Solids 1998, 59:1241-1249.

31. Liu Q, Guo D, Chen K et al. Stabilizing the metastable γ phase in Ga_2O_3 thin films by Cu doping. *J. Alloys Compd.* 2018, 721: 1225-1229.
32. Durst AC, Bhatt RN, Wolff PA Bound magnetic polaron interactions in insulating doped diluted magnetic semiconductors[J]. *Phys. Rev. B* 2002, 65: 235205.
33. Coey JMD, Venkatesan M, Fitzgerald CB Donor impurity band exchange in dilute ferromagnetic oxides[J]. *Nat. Mater.* 2005, 4: 173-179.
34. López-Urías F, Díaz-Ortiz A Magnetism and the electronic correlations in Mn clusters[J]. *J. Alloys Compd.* 2004, 369:117-120.
35. Singh S, Khare N Defects/strain influenced magnetic properties and inverse of surface spin canting effect in single domain CoFe_2O_4 nanoparticles[J]. *Appl. Surf. Sci.* 2016, 364:783-788.
36. Zhou JP, He HC, Nan CW Effects of substrate temperature and oxygen pressure on the magnetic properties and structures of CoFe_2O_4 thin films prepared by pulsed-laser deposition. *Appl. Surf. Sci.* 2007, 253: 7456-7460.

List of Figure Captions

FIGURE 1 (a) TG and DSC curves of the GaMn-polymers in the air. (b) The digital photos of the GMO films grown on the sapphire substrates. (c) 3D AFM images of the GMO films grown on the sapphire substrates. (d) XRD patterns of the PAD-grown GMO-air, GMO- O_2 and undoped $\beta\text{-Ga}_2\text{O}_3$ films on the *c*-plane sapphire. The inset is the enlarged view of XRD patterns around 38° .

FIGURE 2 (a) Cross-sectional HRTEM image of GMO-air film. (b) Spherical aberration TEM image of GMO-air film. (c) Cross-sectional high-resolution TEM image of GMO-O₂ film. (d) Spherical aberration TEM image of GMO-O₂ film. The insets show the corresponding FFT.

FIGURE 3 O 1s peaks of (a) GMO-air and (b) GMO-O₂. Mn 2p peaks of (c) GMO-air and (d) GMO-O₂. (e) The doping concentrations of different Mn ions and the area ratio of V_{O_s}-related peak in the GMO films. (f) The schematic diagram of formation of Mn²⁺, Mn³⁺ and Mn⁴⁺ ions in Ga₂O₃.

FIGURE 4 (a) Optical transmittance spectra of the GMO films. Inset is the $(ah\nu)^2$ versus $h\nu$ plot. (b) Room-temperature PL spectra of the GMO films excited at 250 nm. (c) M-H curves of the GMO films at 300 K. (d) Temperature-dependent magnetization of the GMO films. (e) Schematic of bound magnetic polarons in the GMO films.

Author contributions

Xu Dai prepared the samples and performed the experiments; Xi Zhang provided the resources and supervised the project; Xu Dai, Xi Zhang and Gang Xiang wrote the paper. Gang Xiang designed and supervised the project. All authors contributed to the general discussion.